Influence of depressed road configuration on downwind pollutant concentrations: a CFD study under various thermal stability conditions

Nicolas Reiminger[1,2*], Xavier Jurado[1], Loïc Maurer[2], José Vazquez[2], Cédric Wemmert[2]

[1]*AIR&D, 67000, Strasbourg, France*
[2]*ICUBE Laboratory, CNRS/University of Strasbourg, 300 Bd. Sébastien Brant, 67400 Illkirch-Graffenstaden, France*

[*]*Corresponding author: Tel. +33 (0)6 31 26 75 88, Mail. nreiminger@air-d.fr*

Citation : Reiminger, N., Jurado, X., Maurer, L., Vazquez, J., & Wemmert, C. (2023). Influence of depressed road configuration on downwind pollutant concentrations: A CFD study under various thermal stability conditions. Journal of Wind Engineering and Industrial Aerodynamics, 235, 105361. https://doi.org/10.1016/j.jweia.2023.105361

Abstract: Outdoor air quality is a major concern worldwide, especially in urban areas. In this paper, the influence of depressed roads (specific road designs where the road's surface is lower than the surrounding ground level) on the downwind pollutant concentration was assessed using a validated Computational Fluid Dynamics (CFD) solver, for eight road depths (D) and thirteen stability conditions (Richardson numbers, Ri). Depressed roads can decrease downwind pollutant concentrations compared to classical roads, but only under neutral and unstable thermal conditions. Under neutral thermal condition, a threshold is reached for D = 0.375, leading to a maximal pollution reduction of around 10% at pedestrian level and around 5% at the first-floor level. In such stability conditions, pollutant concentrations are lower as D increases and Ri decreases. Under stable conditions, such roads lead to higher pollutant concentrations. Four equations allowing to predict the downwind pollutant concentrations are given depending on the distance from the road centerline, the road depth, and the thermal stability condition. The results of this study provide pre-construction guidance on whether a depressed road should be considered to protect human health, as well as predictive tools to assess the beneficial or adverse impact of such structures on air quality.

1. Introduction

Outdoor air pollution has significant adverse effects on human health (Chen et al., 2012; Fenech and Aquilina, 2020; Hamra et al., 2014; Nuvolone et al., 2018), and was the cause of around 4.2 million premature deaths worldwide in 2016 (WHO, 2016). In the same year, approximately 500,000 people died prematurely in Europe (EEA, 2019), a number that did not decrease in 2018 (EEA, 2020). Nowadays, people are increasingly living in urban areas (more than 50% around the world, and 74% in Europe) with a percentage expected to reach 68% worldwide in 2050 (United Nations, 2019). In such areas, air quality can be very poor due to high anthropogenic emissions such as traffic-related emissions (Belalcazar et al., 2009; Delmas et al., 1997; Wei et al., 2021), resulting in a higher health risk for people living near heavy traffic roads (Chen et al., 2017; Finkelstein et al., 2004; Petters et al., 2004). Based on these findings, air quality has become a major global challenge, and the greatest environmental risk in Europe (EEA, 2020).

Following the current European Union (EU) legislation with the "Directive/2008/50/EC" (EU, 2008), as well as the World Health Organization (WHO) guidelines (WHO, 2017, 2005) recently updated (WHO, 2021), air quality regulations are increasing in Europe, and actions are taken. Therefore, outdoor air quality in European cities is expected to improve in the next decades with the decrease of emissions and air pollutant concentrations (European Commission, 2013). However, time is needed for these actions to achieve significant results, and, in the meantime, people are still living in areas where outdoor air quality is poor. Therefore, it is essential to (a) continue assessing air quality in urban areas, (b) understand the phenomena and processes that govern air pollution dispersion, and (c) find ways to reduce human exposure to airborne pollution in these locations.

Air quality assessment in cities is generally performed either through the use of sensors or modelling. While the former approach is time consuming and requires gathering enough data to be exploited and compared to EU and WHO standards (Bai et al., 2020; Jurado et al., 2020), the second one allows to widen the scope of possibilities (e.g., assessing the impact of changes in traffic, building/land morphologies, etc.) in a prospective purpose (Baklanov and Zhang, 2020; Yang et al., 2020). Various spatial scales can be considered, from mesoscale (< 200 km) to microscale (< 2 km) and building scale (< 100 m) (Toparlar et al., 2017), each with more suitable models (Leelőssy et al., 2014). Among the several types of existing models, Computational Fluid Dynamics (CFD) is widely used for air quality assessment (Chouak et al., 2022; Kia et al., 2022; Liu et al., 2022), particularly in urban areas (Idrissi et al., 2018; Kluková et al., 2021; Sanchez et al., 2017; Santiago et al., 2019; Trindade da Silva et al., 2021; Zheng et al., 2021), and can be used to compute mean annual concentrations to compare with EU and WHO regulatory standards in cities (Reiminger et al., 2020b; Rivas et al., 2019; Solazzo et al., 2011). CFD is preferred for urban areas modelling because of the complex phenomena that can be considered while other models, such as the Gaussian ones, can lead to poor results under non-flat terrains (Kumar et al., 2015) or in built-up areas (Bady, 2017). Lastly, it should be noted that artificial intelligence-based modelling is emerging for air quality assessment in urban areas (Jurado et al., 2022) with the aim of replacing or improving CFD modelling in the future for air quality purposes (Calzolari and Liu, 2021). They are in early stages, nonetheless, and more in-depth work still needs to be done.

The influence of urban morphology on atmospheric pollution has been well studied through CFD modelling in recent decades. It includes the impact of building aspect ratios in both symmetrical and asymmetrical street canyons (Reiminger et al., 2020c; Santiago and Martin, 2005; Soulhac et al., 2001), as well as the influence of thermal effects (Haghighat and Mirzaei, 2011; Nazarian and Kleissl, 2015; Wang et al., 2014) and chemical mechanisms (Gonzalez Olivardia et al., 2019; Sanchez et al., 2016). However, although many studies have been conducted, there are still issues that have

not been fully explored, such as the influence of depressed roads on downstream pollutant concentrations, which is a type of road design where the road's surface is lower than the surrounding ground level, often used to minimize the visual and noise impact on the surrounding area (Jonasson, 1972).

The aim of this study is to assess the influence of such roads on downstream pollutant concentrations depending on the road configuration and the thermal stability condition. Specifically, CFD simulations are used to assess the evolution of downwind pollutant concentrations as a function of the distance from a road, for several road depths and atmospheric stability conditions (unstable, neutral, and stable atmospheres). The present work is limited to the cases of depressed roads with vertical sidewalls, so no roads with sloping sidewalls are investigated in this study.

2. Description of the study

2.1. Studied cases

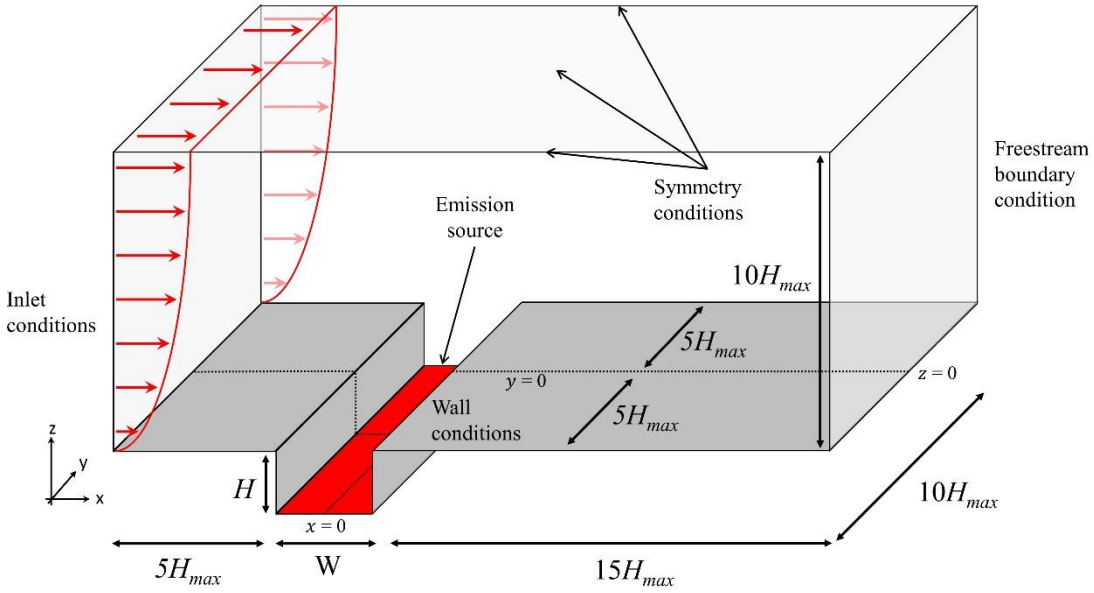

Figure 1. Sketch of the computational domain with the source of emissions (in red), and the ground and the depressed road sidewalls (in gray).

The first focus of the study is the influence of depressed road depth on the pollutant concentrations downwind. To assess this influence, several depressed road configurations were considered. Figure 1 shows the general sketch of the depressed roads modelled in this study. The road configuration is defined by two parameters: W, the width of the road, and H, the height of the sidewalls. The depressed road depth D is then defined as the ratio between the height of the sidewalls and the road width according to equation (1). Throughout this study, W remains unchanged (W = 10 m) and H varies between 0 and 10 m (H_{max} = 10 m).

$$D = \frac{H}{W} \qquad (1)$$

with D the depressed road depth [-], H the sidewalls height [m] and W the road width [m].

Then, the study focuses on the influence of thermal stability conditions. In this paper, thermal effects are quantified using the Richardson number Ri representing the importance of the natural convection (due to thermal effects) relative to the forced convection (due to wind). The corresponding equation taken from Woodward (1998) is given in equation (2). This dimensionless number is also an indicator of the thermal stability with $Ri < 0$, $Ri = 0$ and $Ri > 0$ corresponding to unstable, neutral (isothermal) and stable atmospheres respectively.

$$Ri = \frac{gH_{ref}}{U_{H_{ref}}^2}\frac{(T_H - T_w)}{T_{air}} \qquad (2)$$

with Ri the Richardson number [-], g the gravitational acceleration [m.s^{-2}], $U_{H_{ref}}$ the reference velocity at $z = H_{ref} = 10$ m from the ground [m.s^{-1}], H_{ref} the reference height [m], T_{air} the ambient air temperature [K], T_w the temperature of the heated surfaces [K] and T_H the mean air temperature at $z = H_{ref}$ [K].

This study required a total of 51 simulations and a summary of the cases considered is given in Table 1 with the corresponding road depths (D) and Richardson numbers (Ri).

Table 1. Summary of the cases considered as function of the road depth (D) and the Richardson number (Ri) with the corresponding type of stability conditions according to Woodward (1998).

Ri [-] / *D* [-]	-1	-0.8	-0.6	-0.4	-0.3	-0.2	-0.1	0.0	0.2	0.4	0.6	0.8	1.0
0	●	●	●	●		●		●	●	●	●	●	●
0.125	●	●	●	●		●		●	●	●	●	●	●
0.2								●					
0.25	●	●	●	●	●	●	●	●	●	●	●	●	●
0.375						●		●	●				
0.5			●	●		●	●	●	●	●	●	●	●
0.75								●					
1.0								●					

● : very unstable, ● : unstable, ● : slightly unstable, ● : neutral, ● : stable

2.2. Additional recurring parameters

The dimensionless distance from the road centerline x^* and the dimensionless altitude z^* are respectively defined by equations (3) and (4). It should be noted that $z^* = 0$ corresponds to the ground-level upstream and downstream of the depressed road.

$$x^* = \frac{x}{W} \qquad (3)$$

$$z^* = \frac{z}{W} \qquad (4)$$

with x^* and z^* the dimensionless distance from the road centerline and the altitude respectively [-], x and z the dimensioned distance from the road centerline and the altitude respectively [m] and W the width of the road [m].

The concentration results of the study are given in a dimensionless form following equation (5).

$$C^* = \frac{C.U_{H_{ref}}.H_{ref}}{Q/L} \qquad (5)$$

with C^* the dimensionless pollutant concentration [-], C the pollutant concentration [g.m^{-3}], $U_{H_{ref}}$ the reference velocity at $z = H_{ref} = 10$ m from the ground [m.s^{-1}], H_{ref} the reference height [m], and Q/L the source strength of emissions [g.s^{-1}.m^{-1}].

Lastly, the relative error on concentrations is defined as the following equation:

$$RE = \left(\frac{C^*_{th} - C^*_{pred}}{C^*_{th}}\right) \times 100 \qquad (6)$$

with RE the relative error [%], C^*_{th} the theoretical value of the dimensionless concentration [-] and C^*_{pred} the predicted value of the dimensionless concentration [-].

3. Modelling approach

3.1. Software and calculation methodology

Simulations were performed using OpenFOAM 9 working in parallel calculation on a 16-core Intel® Xeon(R) CPU E5-2670 2,60GHz computing machine under Ubuntu 20.04.4 LTS. The solver used is the *buoyantPimpleFoam* solver, a transient mixed convection solver able to resolve the compressible Navier-Stokes equations for buoyant and turbulent flows. This solver, modified to also account for pollutant dispersion, has already been validated in a previous study (Reiminger et al., 2020a). The performance of the solver was assessed on both velocity and concentration fields using experimental data of a complex 3D situation, under highly unstable conditions. The differences between the experimental and the numerical results were less than 6% on both velocity and concentration fields (Reiminger et al., 2020a).

The Unsteady Reynolds-Averaged Navier-Stokes (URANS) methodology was used to solve the equations, since transient calculation led to equivalent or substantially better results than steady calculation (Tominaga and Stathopoulos, 2017). The use of a RANS methodology induces a new term in the Navier-Stokes momentum equation, the Reynolds stress tensor, requiring the choice of a turbulence closure scheme. Among the various existing turbulence models, the Renormalization Group (RNG) k-ε model presented by Yakhot et al. (1992) has been selected to solve the Reynolds stress tensor. This model has been chosen because it leads to significant improvements over the standard k-ε model (Papageorgakis and Assanis, 1999), while much more complex models such as the anisotropic Reynolds Stress Model (RSM) may not improve the results for higher calculation costs (Koutsourakis et al., 2012).

3.2. Governing equations

3.2.1. Compressible Navier-Stokes equations

The compressible Navier-Stokes equations solved by the *buoyantPimpleFoam* solver are the following, with (7) the continuity, (8) the momentum and (9) the energy equation:

$$\frac{\partial \rho}{\partial t} + \nabla.(\rho u) = 0 \qquad (7)$$

$$\rho\left(\frac{\partial u}{\partial t} + u.\nabla u\right) = -\nabla p + \nabla.\ \left(2\mu_{eff} D(u)\right) - \nabla\left(\frac{2}{3}\mu_{eff}(\nabla.u)\right) + \rho u \qquad (8)$$

$$\frac{\partial \rho e}{\partial t} + \nabla.(\rho u e) + \frac{\partial \rho K}{\partial t} + \nabla.(\rho u K) + \nabla.(up) = \nabla.\left(\alpha_{eff} \nabla e\right) + \rho g.u \qquad (9)$$

$$D(u) = \frac{1}{2}[\nabla u + (\nabla u)^T] \qquad (10)$$

$$K \equiv |u|^2/2 \qquad (11)$$

with ρ the density [kg.m^{-3}], u is the velocity [m.s^{-1}], p the pressure [kg.m^{-1}.s^{-2}], e the thermal energy [m^2.s^{-2}], $D(u)$ the rate of strain tensor given in (10), K the kinetic energy given in (11) [m^2.s^{-2}], g the gravitational acceleration [m.s^{-2}], μ_{eff} the effective viscosity defined as the sum of molecular and turbulent viscosity [kg.m^{-1}.s^{-1}] and α_{eff} the effective thermal diffusivity defined as the sum of laminar and turbulent thermal diffusivities [kg.m^{-1}.s^{-1}].

3.2.2. Passive scalar transport

The transient solver used for this work does not allow to model the dispersion of air pollutants natively. Thus, the advection-diffusion equation (12) governing passive scalar transport has been coded in the solver since no chemical reactions were considered in this study. The corresponding equation is the following:

$$\frac{\partial C}{\partial t} + \nabla.(uC) - \nabla.\left[\left(D_m + \frac{\nu_t}{Sc_t}\right)\nabla C\right] = E \qquad (12)$$

with C the pollutant concentration [kg.m^{-3}], D_m the molecular diffusion coefficient [m^2.s^{-1}], ν_t the turbulent diffusivity [m^2.s^{-1}], Sc_t the turbulent Schmidt number [-] and E the volumetric source term of pollutants (i.e., the emissions) [kg.m^{-3}.s^{-1}].

The turbulent Schmidt number Sc_t is defined as the ratio between the turbulent viscosity ν_t and the turbulent diffusivity D_t. This number, well studied by the scientific community, is ranging between 0.2 and 1.3 for atmospheric dispersion and must be chosen carefully depending on the type of flow studied (Tominaga and Stathopoulos, 2007). According to Yuan et al. (2017), the best turbulent Schmidt number for flows in urban areas is around 0.7, which agrees with others works on pollutant dispersion in the built environment (Rivas et al., 2019; Tominaga and Stathopoulos, 2017; Wang and McNamara, 2006). Thus, a turbulent Schmidt number of 0.7 has been used for this study.

3.3. Computational domain and boundary conditions

Three-dimensional simulations were performed considering all the recommendations concerning domain size and boundary conditions given by Franke et al. (2007). With H_{max} = 10 m, the maximal road sidewall height considered, the inlet boundary is located $5H_{max}$ before the road, where the velocity (13) and turbulence (14-15) are specified according to Richards and Hoxey (1993) and Richards and Norris (2011), using a perpendicular wind direction of 4 m.s^{-1} at 10 m high and a fixed temperature of 293 K. The outlet boundary is located $15H_{max}$ after the road, where a free stream condition is applied to allow a fully development of the flow. The lateral boundaries are placed at $10H_{max}$ from each other and a symmetry condition is used, as for the upper boundary which is located $10H_{max}$ from the ground. No-slip conditions (U = 0 m.s^{-1}) are applied for all the remaining boundaries (the ground, the road, and the road sidewalls), where a fixed temperature depending on the case studied is applied (see Table 2) to account for various thermal stabilities. Traffic exhausts are lastly modelled by a volumetric source along the road on the whole lateral distance of the domain, with a

width of W = 10 m (the width of the road), and over one mesh height (0.25 m). A mass flow rate of 1 g.s^{-1} is used for all the simulations performed.

$$U = \frac{u_*}{\kappa} ln\left(\frac{z + z_0}{z_0}\right) \qquad (13)$$

$$k = \frac{{u_*}^2}{\sqrt{C_\mu}} \qquad (14)$$

$$\varepsilon = \frac{{u_*}^3}{\kappa . z} \qquad (15)$$

with U the wind velocity [m/s], k the turbulent kinetic energy [m^2.s^{-2}], ε the turbulence dissipation rate [m^2.s^{-3}], u_* the friction velocity [m/s], κ the von Kármán constant [-] taken to 0.41, z the altitude [m], z_0 the roughness height [m] taken as 0.5 m to stand for suburbs and built-up areas (Hahmann et al., 2015; Troen and Petersen, 1989), and C_μ a CFD constant [-] taken as 0.085.

Table 2. Temperature conditions as a function of the Richardson number considered.

Ri [-]	-1	-0.8	-0.6	-0.4	-0.3	-0.2	-0.1	0.0	0.2	0.4	0.6	0.8	1.0
Air temperature [K]	293												
Surface temperature [K]	340.8	331.2	321.7	312.1	307.3	302.6	297.8	293.0	283.4	273.9	264.3	254.8	245.2

3.4. Mesh sensitivity tests

Mesh sensitivity tests were carried out considering successive simulations performed with different mesh sizes and the Grid Convergence Index (GCI) methodology was used to assess the mesh-related errors. Mean GCIs of less than 1% were obtained when comparing the results from mesh sizes of 0.5 m and 0.25 m in the area of interest (see Figure S1 in the supplementary materials for more details), which is consistent with other works performed in analogous situations (Reiminger et al., 2020a). Thus, mesh size of 0.5 m is sufficient to ensure fully mesh-independent results and has then been used in this study to avoid excessive calculation costs. Greater refinement of 0.25 m was applied for the wall boundaries (ground, road, and road sidewalls), nonetheless, since strong gradients can appear in such areas. Using this mesh size, each simulation led to a total of around 1.6 million meshes, and an example of resulting mesh is given in Figure S2 in the supplementary materials for D = 0.25.

3.4. Numerical settings

All the simulations were performed with second order schemes for all divergent terms, gradients, and Laplacians. The pollutant concentrations and the downwind streamwise velocities were monitored for several locations after the pollutant source, and the results checked to ensure the convergence of each simulation. At the end of the simulations, all the residuals were at least under 10^{-5}.

4. Results and discussions

4.1. Influence of the depressed road configuration under isothermal conditions

4.1.1. General tendencies

The influence of the depressed road configuration on pollutant concentrations downwind has firstly been assessed in isothermal conditions (neutral stability). Figure 2 shows the pollutant concentration evolution as a function of the distance from the road centerline, for four road depths (D = 0, 0.3, 0.375 and 1.0), and two altitudes (or floor levels): z^* = 0.15, corresponding to the pedestrian level, and z^* = 0.3, corresponding to a first-floor level. At z^* = 0.15, pollutant concentrations increase between x^* = 0 and x^* = 0.5 (which corresponds to the area over the road), and then, decrease quickly with the distance from the road. At z^* = 0.3, concentrations are the highest around x^* = 1.0, and then, decrease with the distance, but more slowly than at z^* = 0.15. The concentrations are on average twice as low at z^* = 0.3 compared to z^* = 0.15.

The results also indicate that increasing the road depth leads to lower pollutant concentrations at pedestrian level (z^* = 0.15), as it can be seen in Figure 2 (A). Indeed, according to the results, pollutant concentrations are overall around 10 % lower for D = 0.375 compared to D = 0 (no depressed road). This observation remains valid until D = 1.0, indicating that there is a threshold effect. The same threshold effect is observed at z^* = 0.3, but to a lesser degree resulting in overall lower pollutant concentrations of around 5%.

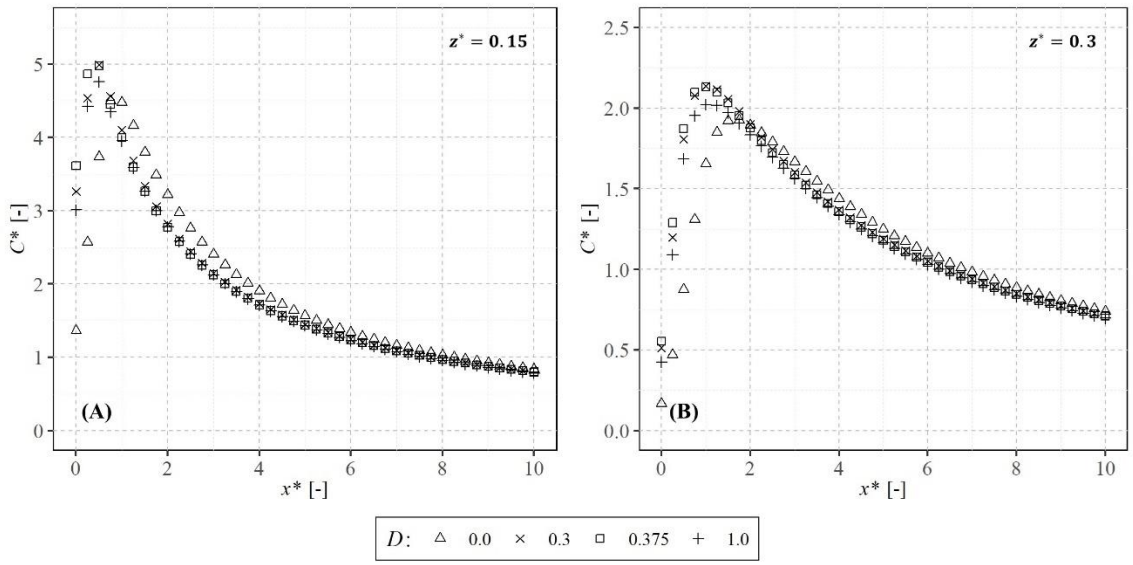

Figure 2. Evolution of the dimensionless pollutant concentration (C^*) as a function of the dimensionless distance from the road centerline (x^*) at (A) z^* = 0.15 m and (B) z^* = 0.3 m for four road depths (0, 0.3, 0.375 and 1) and isothermal conditions (Ri = 0).

To find the origin of this threshold effect, vertical slices of the pollutant concentrations were studied, as well as the streamlines inside the depressed roads and the results are given in Figure 3. According to the results, the vortices induced in the depressed roads are different depending on the road depth considered. There is, for example, two main vortices for D = 0.2 while there is only one main vortex for D = 0.75. Globally, for shallow depressed road (D = 0.125), two vortices appear at the ends of the canyon

shaped by the depressed road; then, these two vortices are getting closer and greater with the increase of the road depth (D = 0.2 and 0.25), the leeward vortex being the greatest; finally, when they are close enough (D = 0.375, 0.75 and 1.0), the vortices merge to create a large-centered vortex. Lastly, it should be noted that the obtained vortex for D = 0.3 seems to be an intermediary state between one and two vortices. Indeed, although a single vortex is observed, the remnants of the two vortices are still apparent according to the "peanut shape" of the streamlines.

By combining the results discussed previously, the pollutant concentrations downwind the depressed road decrease with the increase of road depth under neutral stability conditions, until becoming constant when a main truly circular vortex appears in the canyon, for D = 0.375.

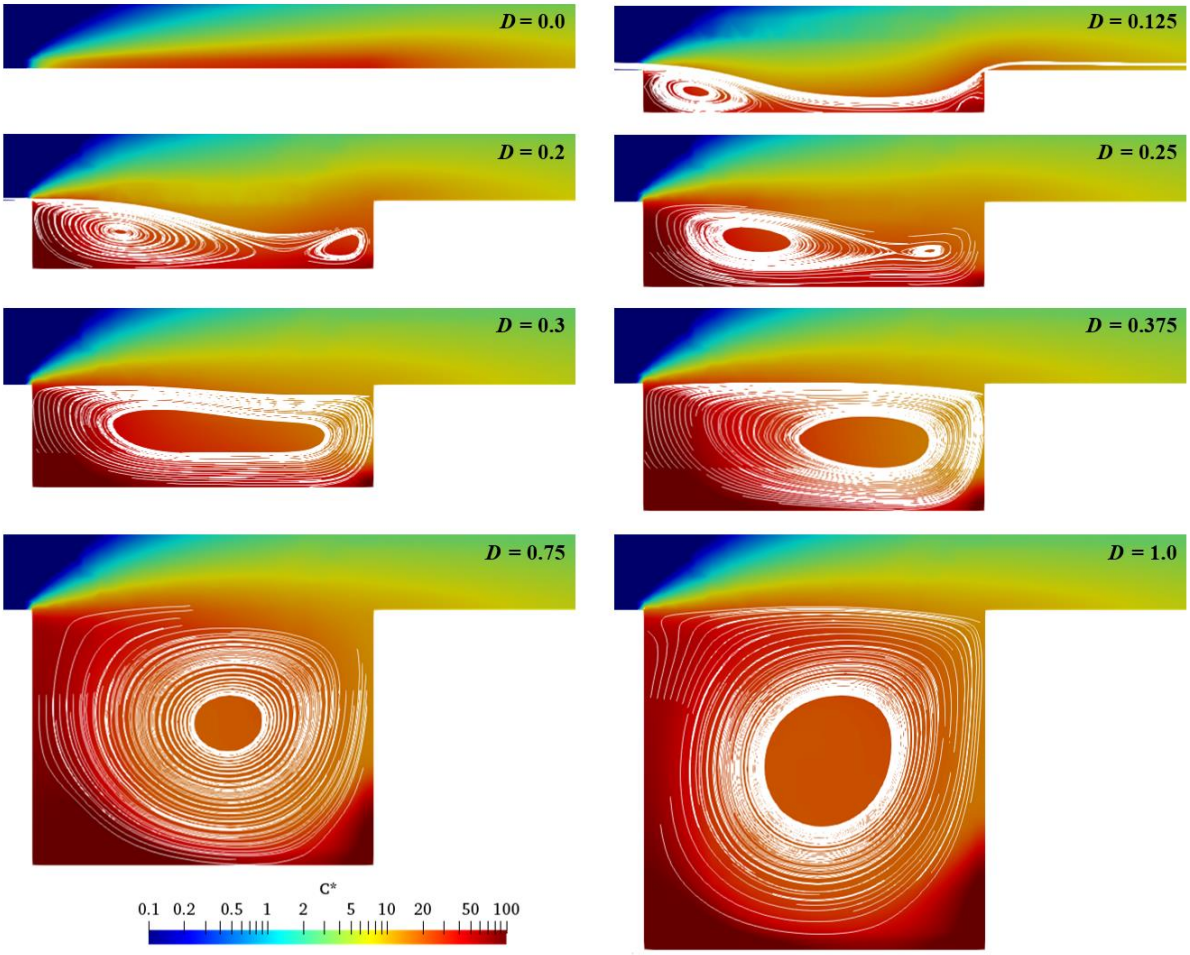

Figure 3. Heatmap of the dimensionless pollutant concentration (C^*) in the depressed road for eight road depths (D = 0, 0.125, 0.2, 0.25, 0.3, 0.375, 0.75 and 1) and isothermal conditions (Ri = 0) with the corresponding streamlines.

4.1.2. Predicting downwind pollutant concentrations under isothermal conditions

An interpolation function able to reproduce the downwind concentration evolution as a function of the distance from the road centerline has been found. This function is derived from the Weibull distribution (16) and is given in equation (17). This function is valid from $x^* \geq 1$ and $x^* \geq 1.5$ for z^* = 0.15 and z^* = 0.3 respectively.

$$f(x) = \frac{k}{\lambda}\left(\frac{x}{\lambda}\right)^{k-1} e^{-(x/\lambda)^k} \qquad (16)$$

with x the variable of interest, k the shape parameter and λ the scale parameter of the distribution (k and λ being positive).

$$C^*(x^*; z^*; D) = \alpha(z^*; D).\beta(z^*).x^{*\gamma(z^*)-1}.\exp\left(-[x^*/\delta(z^*)]^{\gamma(z^*)}\right) \qquad (17)$$

with $C^*(x^*; z^*; D)$ the dimensionless pollutant concentration [-], $\alpha(z^*; D)$ a scale parameter depending on the depressed road depth D and the dimensionless altitude z^* [-], x^* the dimensionless distance from the road centerline [-], z^* the dimensionless altitude where the results are desired (0.15 or 0.3) [-] and $\beta(z^*), \gamma(z^*)$ and $\delta(z^*)$ three constants depending on the dimensionless altitude z^*.

Figure 4 shows an example of interpolation results for D = 0.5 at both z^* = 0.15 and z^* = 0.3 altitudes. As shown in this figure, the interpolation function matches well the modelling results, leading to determination coefficient R^2 of 0.998 and 0.996, and mean relative errors of 2.0 % and 1.8 % at z^* = 0.15 and z^* = 0.3 respectively. Similar interpolation results are obtained for each other road depths considered in this study (i.e., 0.125, 0.2, 0.25, 0.3, 0.375, 0.75 and 1) as well as without a depressed road. Using equation (17), it is therefore possible to continuously calculate the downwind concentrations as a function of the distance from the road centerline, leading to an overall mean (resp. 95th percentile error) of 2.7 % and (resp. 5.6 %) at z^* = 0.15 and 1.9 % and (resp. 3.2 %) at z^* = 0.3. The scale factors $\alpha(z^*; D)$ and the three constants $\beta(z^*), \gamma(z^*)$ and $\delta(z^*)$ necessary to use equation (17) are listed in Table 3 for each road depth modelled in this study. The corresponding mean and 95th percentile relative errors induced by the interpolation function for each considered case are given in Table S1 in the supplementary materials.

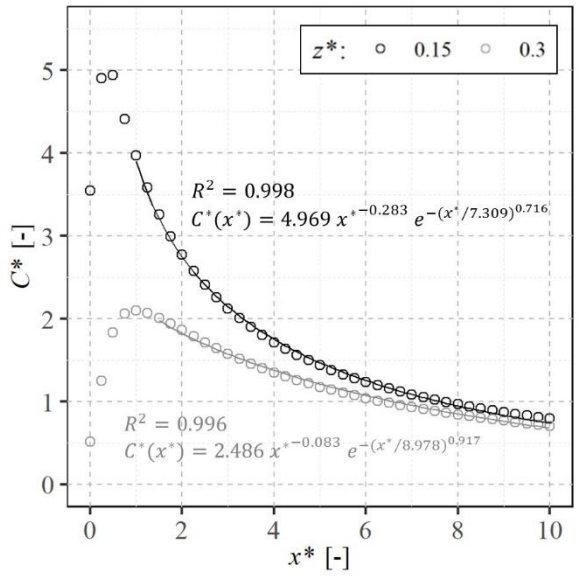

Figure 4. Evolution of the dimensionless pollutant concentration (C^*) as a function of the dimensionless distance from the road centerline (x^*) for a road depth of $D = 0.5$, with the corresponding interpolation functions.

Additionally, another function which allows to assess the scale factor $\alpha(z^*; D)$ as a function of the road depth D has been found. The latter, based on a sigmoid function, is given in equation (18).

$$\alpha(z^*; D) = \frac{a(z^*)}{1 + e^{24.22(D - b(z^*))}} + c(z^*) \qquad (18)$$

with $\alpha(z^*; D)$ the scale parameter depending on the depressed road depth D and the dimensionless altitude z^* [-] and $a(z^*)$, $b(z^*)$ and $c(z^*)$ three constants depending on the dimensionless altitude z^* where the results are desired [-] (a = 3.85, b = 0.22 and c = 28.88 for z^* = 0.15; a = 1.17, b = 0.24 and c = 20.23 for z^* = 0.3).

Table 3. List of the scale factor $\alpha(z^*; D)$ and constants $\beta(z^*), \gamma(z^*)$ and $\delta(z^*)$ to use with equation (17) with the corresponding mean and 95th percentile relative errors.

	z^* = 0.15						z^* = 0.3					
	$\alpha(D)$ [-]	β [-]	γ [-]	δ [-]	RE [%]	P95 RE [%]	$\alpha(D)$ [-]	β [-]	γ [-]	δ [-]	RE [%]	P95 RE [%]
D = 0	32.681				4.0 %	6.5 %	21.385				1.7 %	3.0 %
D = 0.125	32.427				4.3 %	6.9 %	21.328				1.8 %	2.9 %
D = 0.2	31.207				3.5 %	5.9 %	21.066				2.1 %	3.4 %
D = 0.25	30.121				2.6 %	4.2 %	20.738				2.1 %	3.4 %
D = 0.3	29.387	0.172	0.716	7.309	2.3 %	4.8 %	20.484	0.123	0.917	8.978	2.0 %	3.2 %
D = 0.375	28.956				2.1 %	5.6 %	20.296				1.9 %	3.0 %
D = 0.5	28.919				2.0 %	5.7 %	20.214				1.8 %	3.1 %
D = 0.75	28.879				2.0 %	6.2 %	20.235				1.7 %	3.5 %
D = 1	28.854				2.0 %	4.4 %	20.235				2.1 %	4.0 %

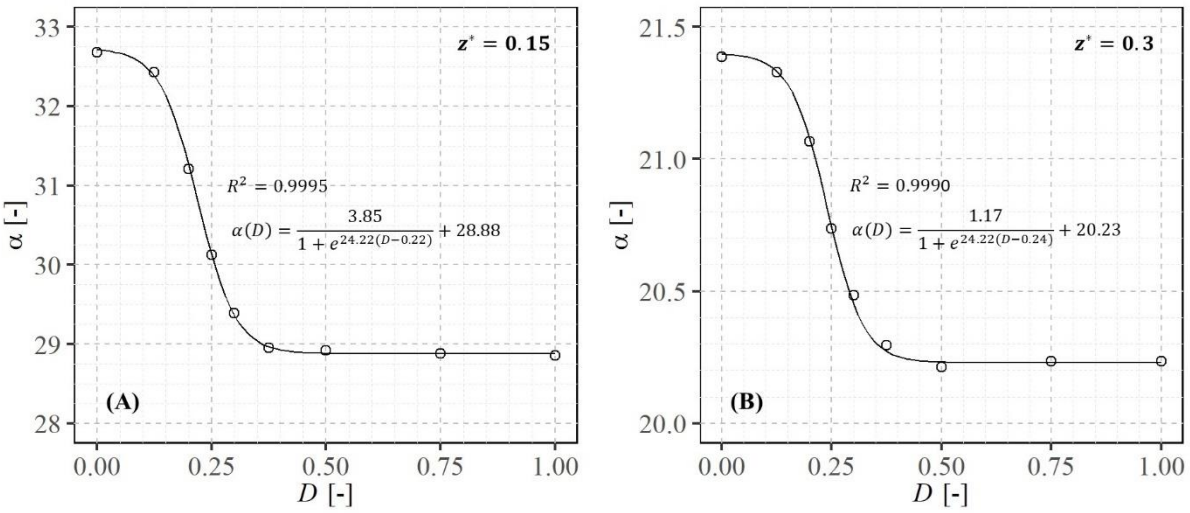

Figure 5. Evolution of the scale factor $\alpha(D)$ as a function of the road depth (D) under isothermal stability conditions at (A) $z^* = 0.15$ and (B) $z^* = 0.3$.

The evolution of the scale factor as a function of the road depth is given in Figure 5 for the two altitudes considered in this work, the solid lines being the results of equation (18). This interpolation function also matches well with the scale factor results for each road depth considered and for both cases of altitude ($R^2 \geq 0.999$). Thus, using equation (18), it is possible to continuously calculate the scale factor as a function of the road depth.

Lastly, by combining equation (17) and (18), it is finally possible to know the downwind concentrations at pedestrian level and first-floor level (respectively at z^* = 0.15 and z^* = 0.3), in neutral stability condition (no thermal effects), and for any depressed road depth ranging between 0 and 1.

Let's take an example where it is desired to predict the downstream pollutant concentration at pedestrian level and 20 m from the road centerline, under a neutral stability condition, for a depressed road of 10 m width and 3.5 m depth. We have, therefore, x^* = 2, z^* = 0.15 and D = 0.35. Using equation (18), we obtain the scale factor α = 29.04. Then, using equation (17), we obtain the dimensionless concentration C^* = 2.76. By using the same process with D = 0, we obtain C^* = 3.11, telling us that with such a depressed road (D = 0.35*)*, we can expect pollutant concentrations of 11% lower, 20 m downwind from the road centerline and under neutral conditions, compared to in absence of depressed road. Note that this example does not include any background concentration or other additional pollutant sources.

4.2. Influence of the thermal stability conditions

4.2.1. General tendencies

The influence of the depressed road configuration on pollutant concentrations downwind has then been assessed considering thermal stability conditions (stable and unstable atmospheres). Examples of results obtained depending on the thermal stability conditions are given in Figure 6. This figure shows the evolution of the downwind concentrations as a function of the distance from the road centerline for the two altitudes considered in this study and five Richardson numbers (-0.4, -0.2, 0, 0.2 and 0.4) considering a road depth of D = 0.25. According to the results, the thermal stability has a great impact on the pollutant concentrations downstream. Indeed, the concentrations are on average 1.8 times higher for Ri = 0.2 and 2.6 times higher for Ri = 0.4 (stable cases) compared to Ri = 0 (isothermal case), while there are on average almost four times as low for Ri = -0.2 and even more for Ri = -0.4 (unstable cases) compared to the neutral case. This observation is true for both z^* = 0.15 and z^* = 0.3.

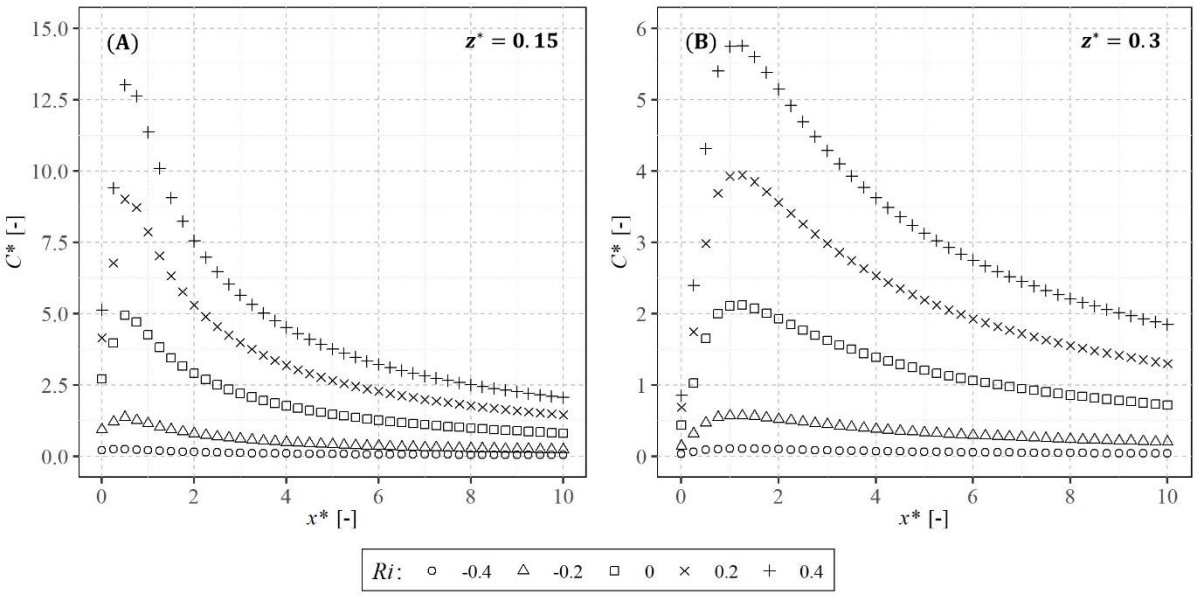

Figure 6. Evolution of the dimensionless pollutant concentration (C^*) as a function of the dimensionless distance from the road centerline (x^*) for a road depth of $D = 0.25$ and various Richardson numbers (Ri) at (A) $z^* = 0.15$ and (B) $z^* = 0.3$.

The origin of these great variations came from changes in the vortices located inside the depressed road (see illustrations in Figure 7), these changes being induced by the thermal effects. Indeed, for D = 0.25, the two main vortices obtained in neutral condition (Ri = 0) become a single main vortex in unstable condition (Ri = -0.2) whereas the stable condition (Ri = 0.2) preserves the two vortices and enlarges them. Inversely, when a single vortex is obtained under neutral conditions, as for D = 0.375, an unstable condition preserves the single vortex while a stable condition leads to two vortices.

To conclude, not only does the depth of the road modify the vortices within the depressed road and, consequently, the downstream concentrations, but also the stability condition induced by thermal effects. Stable conditions tend to the development of two vortices (higher downwind concentrations) while unstable conditions tend to the development of a single vortex (lower downwind concentrations).

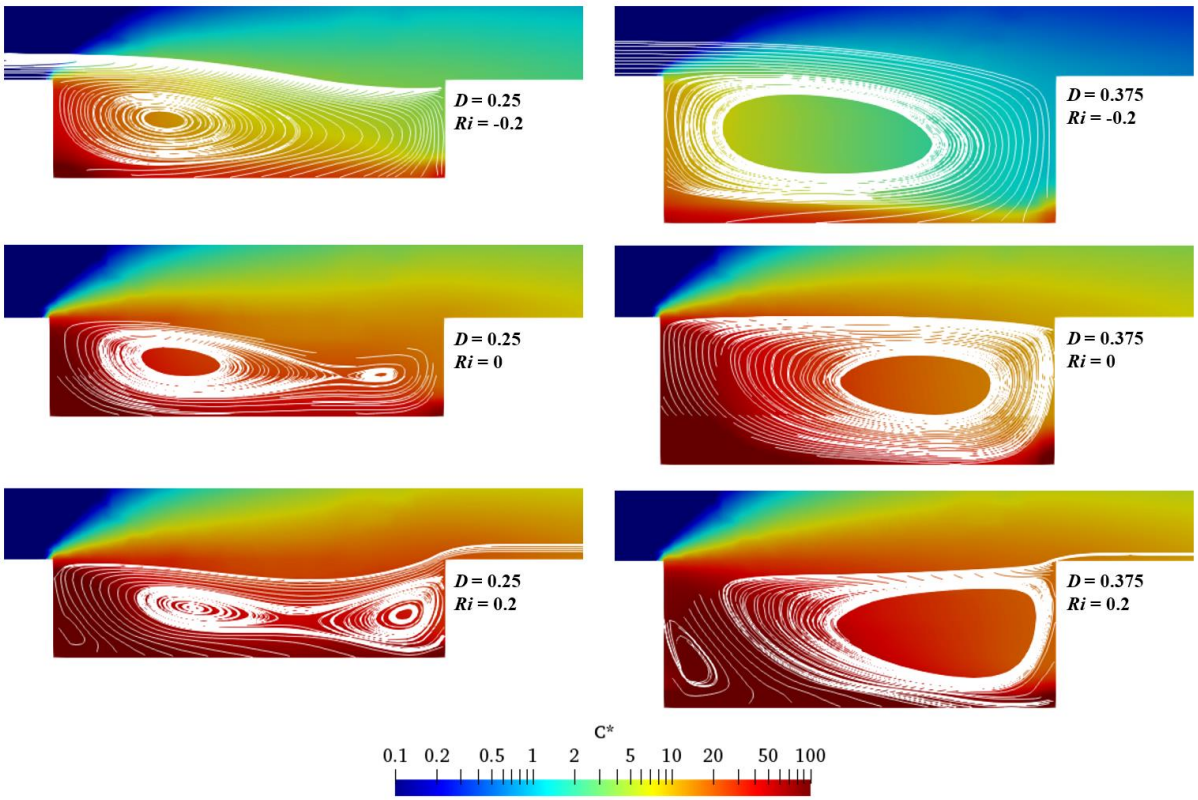

Figure 7. Heatmap of the dimensionless pollutant concentration (C^*) in the depressed road for two road depths (D = 0.25 and D = 0.375) and three Richardson numbers (Ri = -0.2, 0 and 0.2) with the corresponding streamlines.

4.2.2. Predicting downwind pollutant concentrations under non-isothermal conditions

A function describing the downwind pollutant concentrations depending on the distance from the road centerline for a neutral stability condition has been presented previously in Section 4.1.2. This function, given in equation (17), can also be used for both stable and unstable thermal conditions, with an overall mean and 95th percentile error of 3.4 % / 6.3 % respectively at z^* = 0.15 and 2.4 % / 5.3 % respectively at z^* = 0.3. For non-neutral stability conditions, only the scale factor $\alpha(z^*; D)$ changes to become dependent on the Richardson number (i.e., the thermal stability condition). Thus, the three constants $a(z^*)$, $b(z^*)$ and $c(z^*)$ remain the same (a = 3.85, b = 0.22 and c = 28.88 for z^* = 0.15; a = 1.17, b = 0.24 and c = 20.23 for z^* = 0.3).

Table 4. List of the scale factor $\alpha(z^*; D\ ; Ri)$ to use with equation (17) for various thermal stability conditions.

	***Ri* [-]**												
	-1	-0.8	-0.6	-0.4	-0.3	-0.2	-0.1	0	0.2	0.4	0.6	0.8	1
z^* **= 0.15**													
D = 0	30.06	30.55	31.05	31.58	-	32.12	-	32.71	33.26	33.86	34.49	35.14	35.82
D = 0.125	1.88	3.42	6.75	13.25	-	22.29	-	32.37	43.08	54.60	67.57	81.37	94.67
D = 0.25	0.06	0.14	0.41	1.56	3.57	8.29	17.52	30.12	54.85	78.07	99.34	115.24	128.75
D = 0.5	-	-	-	-	-	0.68	4.94	28.89	75.15	107.71	124.70	138.54	157.68
z^* **= 0.3**													
D = 0	18.60	19.06	19.53	20.02	-	20.54	-	21.39	21.67	22.26	22.91	23.58	24.30
D = 0.125	1.20	2.19	4.33	8.52	-	14.46	-	21.33	28.75	37.00	46.53	56.93	67.30
D = 0.25	0.04	0.09	0.28	1.05	2.42	5.63	13.31	20.45	37.56	53.87	69.17	81.11	91.86
D = 0.5	-	-	-	-	-	0.47	3.44	20.21	52.54	75.80	88.06	98.68	113.50

The Ri-dependent scale factors $\alpha(z^*; D\ ; Ri)$ for the stable and unstable thermal conditions considered in this study are listed in Table 4. The corresponding mean and 95th percentile relative errors induced by the interpolation function are given in Table S2 and Table S3 in the supplementary materials respectively.

The α parameter is the only variable depending on Ri and D in equation (17). Thus, for a given considered altitude, studying α is equivalent as studying the pollutant concentration evolution downwind. The evolution of the scale factor $\alpha(z^*; D\ ; Ri)$ as a function of the Richardson number Ri has been plotted for the two altitudes considered in this work and four road depths (D = 0, 0.125, 0.25 and 0.5). The results are given in Figure 8. According to this figure, and as a general trend, the downwind pollutant concentrations increase with the Richardson number and inversely. In absence of depressed road (D = 0), the thermal stability condition is only slightly changing the downwind pollutant concentration. In this case, the evolution of α is linearly correlated with the evolution of Ri, and increasing the latter by 0.2 leads to an overall increase in the downwind concentration of 1.75%.

For depressed roads, the changes in downwind pollutant concentrations are much more significant. As an example, for D = 0.25, the downwind pollutant concentrations are overall twice as high for Ri = 0.2 compared to Ri = 0 while they are overall twice as low for Ri = -0.2. The downwind pollutant concentration evolution is no longer linear and became quadratically correlated for a shallow depressed road (D = 0.125). For deeper depressed roads (D = 0.25 and 0.5), the evolution of the downwind pollutant concentrations as a function of the Richardson number is still quadratically correlated but only for Ri > 0 (stable conditions); for unstable conditions (Ri < 0), this evolution follows a sigmoid function.

The equations describing the evolution of the scale factor $\alpha(z^*; D\ ; Ri)$ as a function of the Richardson number and the road depth are given in equation (19) and (20) when following a quadratic or a sigmoid function respectively.

$$\alpha(z^*; Ri\ ;\ D) = A_1 \times Ri^2 + B_1 \times Ri + C_1 \quad (19)$$

$$\alpha(z^*; Ri\ ;\ D) = \frac{A_2}{1 + e^{x.B_2}} + C_2 \quad (20)$$

with $\alpha(z^*; Ri\ D)$ the scale factor depending on the Richardson number and the road depth [-] and A_1, B_1, C_1, A_2, B_2 and C_2 six constants depending on the Richardson number and the road depth [-].

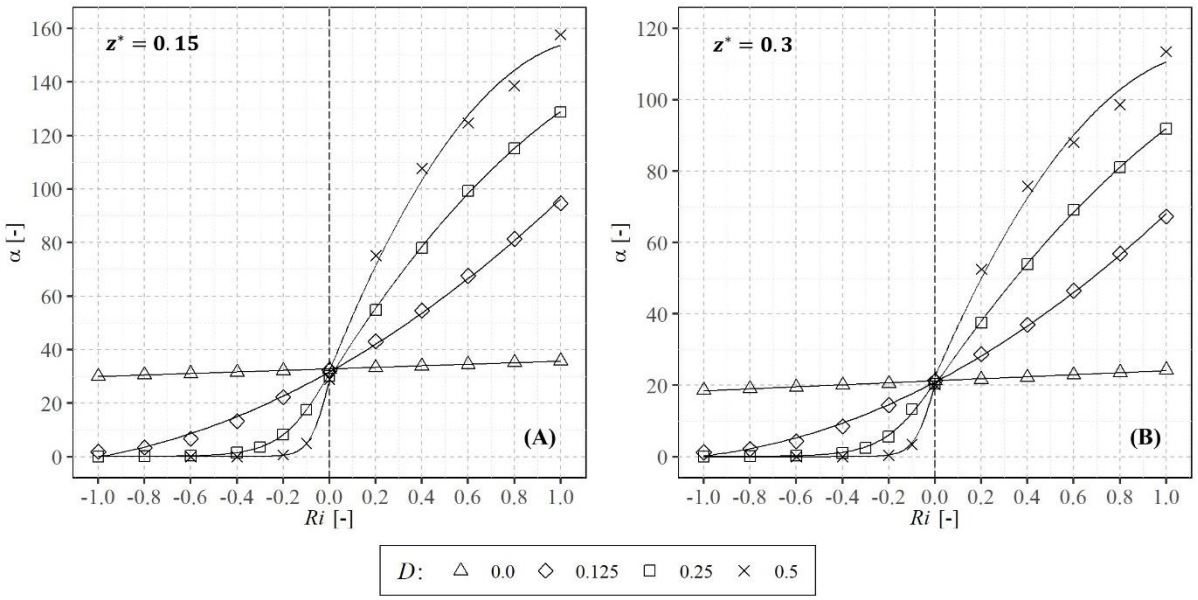

Figure 8. Evolution of the scale factor $\alpha(D; Ri)$ factor as a function of the Richardson number (Ri) for (A) z^* = 0.15 and (B) z^* = 0.3

The equation to be chosen between equation (19) and (20) depends on the thermal stability condition considered as well as the road depth, as shown in Figure 8. Table 5 summarizes which equation should be used for which thermal stability condition with the corresponding constants.

Table 5. Description of the equation to be chosen to calculate the scale factor depending on the thermal stability condition and the corresponding constants.

	Equ. (19)	**Equ. (20)**	A_1	B_1	C_1	A_2	B_2	C_2
z^* = 0.15								
D = 0	●	-	0	2.87	32.79	-	-	-
D = 0.125	●	-	16.42	48.26	31.73	-	-	-
D = 0.25	● if $Ri <$ 0	● if $Ri \geq$ 0	-38.12	137.49	29.63	61.95	-9.38	0.08
D = 0.5	● if $Ri <$ 0	● if $Ri \geq$ 0	-93.98	215.56	32.12	57.00	-23.62	0.05
z^* = 0.3								
D = 0	●	-	0	2.83	21.26	-	-	-
D = 0.125	●	-	13.29	33.96	20.92	-	-	-
D = 0.25	● if $Ri <$ 0	● if $Ri \geq$ 0	-22.00	93.87	20.14	41.64	-8.81	0.04
D = 0.5	● if $Ri <$ 0	● if $Ri \geq$ 0	-61.65	149.81	22.50	40.42	-22.27	0.001

Lastly, by combining equations (17), (18) and (20), it is finally possible to predict the downwind pollutant concentrations at pedestrian level and first-floor level (respectively at z^* = 0.15 and z^* = 0.3), for road depths of 0, 0.125, 0.25 and 0.5 and for any Richardson number ranging between -1 and 1.

Let's take an additional example based on the previous one given in Section 4.1.2. As a reminder, it was previously desired to predict the downstream pollutant concentration at pedestrian level and 20 m from the road centerline for a depressed road of 10 m width and 3.5 m depth. We had, therefore, x^* = 2, z^* = 0.15 and D = 0.35 which led to C^* = 2.76 under neutral conditions. Now, we want to know the impact of thermal effects on this concentration when the wind speed is equal to 3 m.s^{-1} at 10 m high, and when the ground is 10 K colder than the ambient air, leading respectively to a stable thermal condition. According to equation (2), it leads to Ri = 0.37. Equation (19) does not allow to calculate the scale factor for D = 0.35 but allow the calculation for both D = 0.25 and D = 0.5. The corresponding scale factors are 75.3 and 99.0 respectively. Assuming a linear evolution of the scale factor as a function of the road depth, we obtain α = 84.8 for D = 0.35, leading to C^* = 8.06 using equation (17). Thus, we can expect concentrations of around three times higher for the stability condition considered for this example. Note that the obtained result is only an order of magnitude, since we needed to assume a linear evolution of the scale factor for the road depth considered in this example.

4.3. Recommendations for the use of depressed road to mitigate air pollution

The results previously discussed give interesting construction guidance on when considering building a depressed road. Indeed, it was previously shown that the thermal stability condition is a key parameter when considering the construction of a depressed road: while deep depressed roads can lead to lower downwind pollutant concentrations in comparison to shallow depressed roads (or in absence of depressed roads) in both neutral and unstable thermal conditions, they lead to higher downwind concentrations under stable thermal conditions. Thus, depressed roads can be both beneficial and detrimental to downwind air quality.

To bring out the best of depressed road to mitigate downwind pollutant concentrations, the following recommendations can be suggested:

- Depressed roads should be considered when atmospheric stability is mainly neutral or unstable at times of heavy traffic. This case is the most likely case since unstable atmospheres occur generally during the day, when the traffic and, therefore, the emissions are the highest. Thus, by building a depressed road in such case, downstream pollutant concentrations can be highly reduced. During the night, when the stable atmosphere appears, the depressed road will be detrimental for downwind air quality but is not a big issue, nonetheless, since the traffic-related emissions are generally the lowest at this moment.
- Depressed roads should be avoided when stable atmospheres are occurring while the traffic is greatest. In such case, a depressed road will be counterproductive and detrimental the downstream air quality.
- When considering building a depressed road, the road depth should be of at least D = 0.375 to ensure reaching the threshold obtained under neutral stability conditions and maximizing the downwind concentration reduction.
- The equations given to predict the downstream pollutant concentrations as a function of the depressed road depth and the thermal stability condition should be used, prior to construction, to find the best depressed road depth depending on project constraints. It should also be noted that, even if no buildings were considered in this study, these equations can still provide a first estimation of the downwind pollutant concentrations.

5. Conclusion

The influence of depressed road configurations was studied using a validated CFD model. This study considered both numerous road configurations (with various depressed road depth) and thermal stability conditions (stable, neutral, and unstable atmospheres) for a total of 51 simulations performed. Based on the results of these simulations, the main conclusions are as follows:

(a) Under neutral thermal conditions ($Ri = 0$), a depressed road leads to lower downwind pollutant concentrations compared to a classical road. The downwind pollutant concentration decreases with increasing road depth until reaching a threshold for a depressed road depth D of 0.375, beyond which concentrations do not change anymore.

(b) Under unstable thermal conditions ($Ri < 0$), a depressed road leads to lower downwind pollutant concentrations. The downwind pollutant concentrations decrease with increasing road depth, much more significantly than under neutral thermal conditions.

(c) Under stable thermal conditions ($Ri > 0$), a depressed road leads to higher downwind pollutant concentrations. The downwind pollutant concentrations increase with increasing road depth.

(d) The origin of the variations in downwind pollutant concentrations due to thermal effects are changes in the vortices which appear in the depressed road.

(e) Four equations allowing to continuously predict downwind pollutant concentrations as a function of the distance from the road centerline are given.

(f) It is recommended to consider depressed roads to mitigate downwind air pollution when the atmosphere is both mostly neutral/unstable and the traffic is high to avoid counterproductive effects.

6. Limitations of the study and further work

Further work could be considered to increase the effectiveness of depressed roads on the reduction of downwind pollutant concentrations, such as considering solid barriers (e.g., noise barriers) or vegetative barriers. However, considering these new designs, the experiments must include thermal stability conditions given the impact of thermal effects on the air quality benefits of depressed roads. This study only considered idealized cases of depressed roads (vertical sidewalls, no buildings, etc.). Thus, supplementary work could also be done to assess the impact of such new parameters. Studying the influence of depressed roads in the presence of building, with non-vertical sidewalls or with nonconstant surface temperature are some examples of such additional work.

Appendices

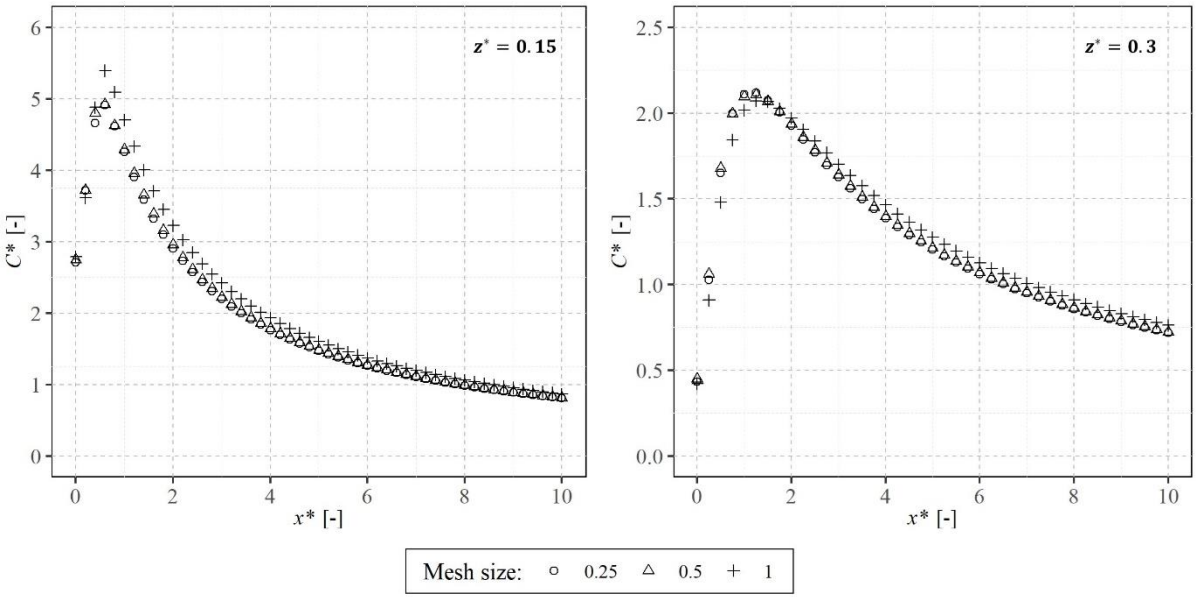

Figure S1. Evolution of the dimensionless pollutant concentration (C^*) as a function of the dimensionless distance from the road centerline (x^*) at z^* = 0.15 m and z^* = 0.3 m and for three mesh sizes (0.25, 0.5 and 1 m).

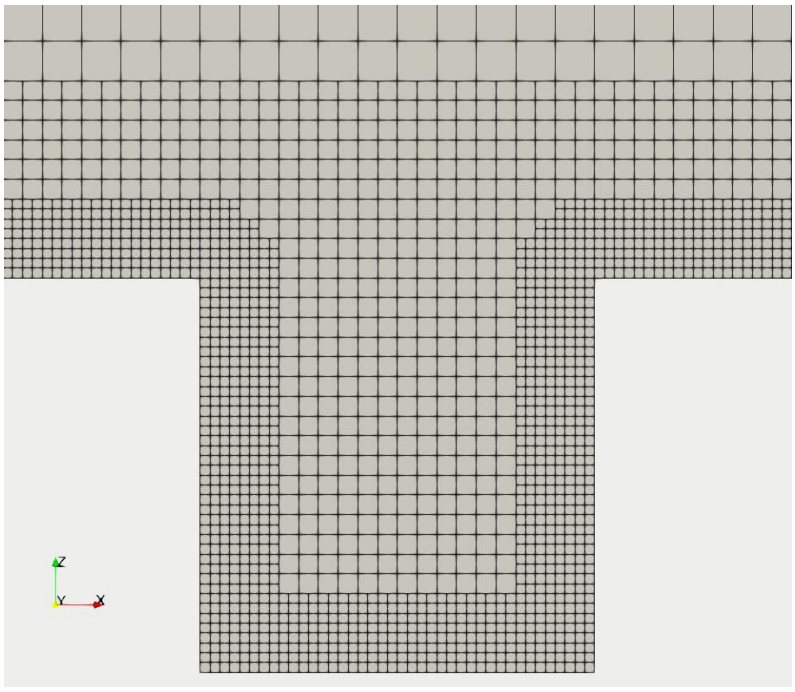

Figure S2. Grid selected for computation (H/W = 1.0 case).

Table S1. Mean and 95th percentile relative errors obtained when using the interpolation function given in equation (17) in neutral stability condition.

	$z^* = 0.15$		$z^* = 0.3$	
	MRE [%]	**P95 RE** [%]	**MRE** [%]	**P95 RE** [%]
$D = 0$	4.0 %	6.5 %	1.7 %	3.0 %
$D = 0.125$	4.3 %	6.9 %	1.8 %	2.9 %
$D = 0.2$	3.5 %	5.9 %	2.1 %	3.4 %
$D = 0.25$	2.6 %	4.2 %	2.1 %	3.4 %
$D = 0.3$	2.3 %	4.8 %	2.0 %	3.2 %
$D = 0.375$	2.1 %	5.6 %	1.9 %	3.0 %
$D = 0.5$	2.0 %	5.7 %	1.8 %	3.1 %
$D = 0.75$	2.0 %	6.2 %	1.7 %	3.5 %
$D = 1$	2.0 %	4.4 %	2.1 %	4.0 %

Table S2. Mean relative errors obtained when using the interpolation function given in equation (17) for various thermal stability condition.

	***MRE* [%]**												
	-1	-0.8	-0.6	-0.4	-0.3	-0.2	-0.1	0	0.2	0.4	0.6	0.8	1
$z^* = 0.15$													
$D = 0$	2.5 %	2.7 %	3.0 %	3.3 %	-	3.6 %	-	4.0 %	4.3 %	4.7 %	5.0 %	5.4 %	5.8 %
$D = 0.125$	1.6 %	1.9 %	2.4 %	3.3 %	-	4.1 %	-	4.3 %	4.6 %	4.6 %	4.7 %	4.8 %	4.9 %
$D = 0.25$	2.8 %	2.5 %	2.2 %	1.8 %	1.8 %	2.0 %	2.3 %	2.6 %	3.1 %	3.6 %	3.9 %	4.2 %	4.4 %
$D = 0.5$	-	-	-	-	-	2.1 %	2.0 %	2.0 %	3.0 %	3.1 %	3.8 %	4.0 %	4.5 %
$z^* = 0.3$													
$D = 0$	2.8 %	2.4 %	2.0 %	1.6 %	-	1.5 %	-	1.7 %	1.5 %	1.6 %	1.9 %	2.3 %	2.9 %
$D = 0.125$	2.5 %	2.0 %	1.6 %	1.4 %	-	1.5 %	-	1.8 %	2.2 %	2.7 %	3.2 %	3.9 %	4.5 %
$D = 0.25$	3.0 %	2.7 %	2.6 %	1.9 %	1.7 %	1.6 %	0.9 %	1.8 %	2.1 %	2.5 %	2.9 %	3.4 %	3.9 %
$D = 0.5$	-	-	-	-	-	1.5 %	1.5 %	1.8 %	3.3 %	3.2 %	3.8 %	4.1 %	5.0 %

Table S3. 95th percentile relative errors obtained when using the interpolation function given in equation (17) for various thermal stability condition.

	95^{th} RE [%]												
	-1	-0.8	-0.6	-0.4	-0.3	-0.2	-0.1	0	0.2	0.4	0.6	0.8	1
z^* = 0.15													
D = 0	4.2 %	4.7 %	5.1 %	5.5 %	-	6.0 %	-	6.5 %	6.8 %	7.3 %	7.8 %	8.2 %	8.7 %
D = 0.125	4.2 %	3.1 %	4.2 %	5.6 %	-	6.6 %	-	6.9 %	7.3 %	7.4 %	7.5 %	7.7 %	7.9 %
D = 0.25	9.0 %	8.3 %	8.1 %	6.3 %	5.7 %	4.7 %	3.9 %	4.3 %	5.3 %	6.0 %	6.5 %	7.0 %	7.2 %
D = 0.5	-	-	-	-	-	7.7 %	7.1 %	5.7 %	5.0 %	5.2 %	6.2 %	6.6 %	7.3 %
z^* = 0.3													
D = 0	7.5 %	6.8 %	6.1 %	5.4 %	-	4.6 %	-	3.0 %	3.0 %	2.6 %	3.2 %	3.9 %	4.6 %
D = 0.125	7.5 %	6.7 %	5.6 %	4.2 %	-	2.9 %	-	2.9 %	3.7 %	4.3 %	5.1 %	6.2 %	7.4 %
D = 0.25	9.1 %	8.7 %	8.5 %	7.0 %	6.3 %	5.4 %	2.2 %	4.3 %	3.4 %	4.0 %	5.0 %	6.0 %	6.9 %
D = 0.5	-	-	-	-	-	5.7 %	4.6 %	3.1 %	5.1 %	5.3 %	6.3 %	6.9 %	8.0 %

References

Bady, M., 2017. Evaluation of Gaussian Plume Model against CFD Simulations through the Estimation of CO and NO Concentrations in an Urban Area. American Journal of Environmental Sciences 13, 93–102. https://doi.org/10.3844/ajessp.2017.93.102

Bai, L., He, Z., Li, C., Chen, Z., 2020. Investigation of yearly indoor/outdoor PM2.5 levels in the perspectives of health impacts and air pollution control: Case study in Changchun, in the northeast of China. Sustainable Cities and Society 53, 101871. https://doi.org/10.1016/j.scs.2019.101871

Baklanov, A., Zhang, Y., 2020. Advances in air quality modeling and forecasting. Global Transitions 2, 261–270. https://doi.org/10.1016/j.glt.2020.11.001

Belalcazar, L.C., Fuhrer, O., Ho, M.D., Zarate, E., Clappier, A., 2009. Estimation of road traffic emission factors from a long term tracer study. Atmospheric Environment 43, 5830–5837. https://doi.org/10.1016/j.atmosenv.2009.07.059

Calzolari, G., Liu, W., 2021. Deep learning to replace, improve, or aid CFD analysis in built environment applications: A review. Building and Environment 206, 108315. https://doi.org/10.1016/j.buildenv.2021.108315

Chen, H., Kwong, J.C., Copes, R., Tu, K., Villeneuve, P.J., van Donkelaar, A., Hystad, P., Martin, R.V., Murray, B.J., Jessiman, B., Wilton, A.S., Kopp, A., Burnett, R.T., 2017.

Living near major roads and the incidence of dementia, Parkinson's disease, and multiple sclerosis: a population-based cohort study. The Lancet 389, 718–726. https://doi.org/10.1016/S0140-6736(16)32399-6

Chen, R., Samoli, E., Wong, C.-M., Huang, W., Wang, Z., Chen, B., Kan, H., 2012. Associations between short-term exposure to nitrogen dioxide and mortality in 17 Chinese cities: The China Air Pollution and Health Effects Study (CAPES). Environment International 45, 32–38. https://doi.org/10.1016/j.envint.2012.04.008

Chouak, M., Cantin, S., Seers, P., Garnier, F., 2022. High-fidelity CFD modeling of pollutant dispersion from aircraft auxiliary power units (APUs) at a realistic airport and the effects on airport air quality. Journal of Wind Engineering and Industrial Aerodynamics 230, 105208. https://doi.org/10.1016/j.jweia.2022.105208

Delmas, R., Serca, D., Jambert, C., 1997. Global inventory of NOx sources. Nutrient Cycling in Agroecosystems 48, 51–60. https://doi.org/10.1023/A:1009793806086

EEA, 2020. Air quality in Europe: 2020 report. Publications Office, LU.

EEA, 2019. Air quality in Europe: 2019 report.

EU, 2008. Directive 2008/50/EC of the european parliament and of the council of 21 May 2008 on ambient air quality and cleaner air for Europe, European Union.

European Commission, 2013. Proposal for a Directive of the European Parliament and of the Council on the reduction of national emissions of certain atmospheric pollutants and amending Directive 2003/35/EC. European Commission (EC), Brussels, Belgium.

Fenech, S., Aquilina, N.J., 2020. Trends in ambient ozone, nitrogen dioxide, and particulate matter concentrations over the Maltese Islands and the corresponding health impacts. Science of The Total Environment 700, 134527. https://doi.org/10.1016/j.scitotenv.2019.134527

Finkelstein, M.M., Jerrett, M., Sears, M.R., 2004. Traffic Air Pollution and Mortality Rate Advancement Periods. American Journal of Epidemiology 160, 173–177. https://doi.org/10.1093/aje/kwh181

Franke, J., Hellsten, A., Schlünzen, H., Carissimo, B., 2007. Best practice guideline for the CFD simulation of flows in the urban environment. COST Action 732.

Gonzalez Olivardia, F., Zhang, Q., Matsuo, T., Shimadera, H., Kondo, A., 2019. Analysis of Pollutant Dispersion in a Realistic Urban Street Canyon Using Coupled CFD and Chemical Reaction Modeling. Atmosphere 10, 479. https://doi.org/10.3390/atmos10090479

Haghighat, F., Mirzaei, P.A., 2011. Impact of non-uniform urban surface temperature on pollution dispersion in urban areas. Build. Simul. 4, 227–244. https://doi.org/10.1007/s12273-011-0035-6

Hahmann, A., Lennard, C., Badger, J., Vincent, C., Kelly, M., Volker, P., Agent, B., Refslund, J., 2015. Mesoscale modeling for the Wind Atlas of South Africa (WASA) project. https://doi.org/10.13140/RG.2.1.3735.6887

Hamra, G.B., Guha, N., Cohen, A., Laden, F., Raaschou-Nielsen, O., Samet, J.M., Vineis, P., Forastiere, F., Saldiva, P., Yorifuji, T., Loomis, D., 2014. Outdoor particulate matter exposure and lung cancer: a systematic review and meta-analysis. Environ Health Perspect 122, 906–911. https://doi.org/10.1289/ehp/1408092

Idrissi, M.S., Lakhal, F.A., Salah, N.B., Chrigui, M., 2018. CFD Modeling of Air Pollution Dispersion in Complex Urban Area, in: Haddar, M., Chaari, F., Benamara, A., Chouchane, M., Karra, C., Aifaoui, N. (Eds.), Design and Modeling of Mechanical Systems—III, Lecture Notes in Mechanical Engineering. Springer International Publishing, Cham, pp. 1191–1203. https://doi.org/10.1007/978-3-319-66697-6_117

Jonasson, H.G., 1972. Diffraction by wedges of finite acoustic impedance with applications to depressed roads. Journal of Sound and Vibration 25, 577–585. https://doi.org/10.1016/0022-460X(72)90479-8

Jurado, X., Reiminger, N., Benmoussa, M., Vazquez, J., Wemmert, C., 2022. Deep learning methods evaluation to predict air quality based on Computational Fluid Dynamics. Expert Systems with Applications 203, 117294. https://doi.org/10.1016/j.eswa.2022.117294

Jurado, X., Reiminger, N., Vazquez, J., Wemmert, C., Dufresne, M., Blond, N., Wertel, J., 2020. Assessment of mean annual NO2 concentration based on a partial dataset. Atmospheric Environment 221, 117087. https://doi.org/10.1016/j.atmosenv.2019.117087

Kia, S., Flesch, T.K., Freeman, B.S., Aliabadi, A.A., 2022. Calculating gas emissions from open-pit mines using inverse dispersion modelling: A numerical evaluation using CALPUFF and CFD-LS. Journal of Wind Engineering and Industrial Aerodynamics 226, 105046. https://doi.org/10.1016/j.jweia.2022.105046

Kluková, Z., Nosek, Š., Fuka, V., Jaňour, Z., Chaloupecká, H., Ďoubalová, J., 2021. The combining effect of the roof shape, roof-height non-uniformity and source position on the pollutant transport between a street canyon and 3D urban array. Journal of Wind Engineering and Industrial Aerodynamics 208, 104468. https://doi.org/10.1016/j.jweia.2020.104468

Koutsourakis, N., Bartzis, J.G., Markatos, N.C., 2012. Evaluation of Reynolds stress, k-ε and RNG k-ε turbulence models in street canyon flows using various experimental datasets. Environmental Fluid Mechanics 12, 379–403. https://doi.org/10.1007/s10652-012-9240-9

Kumar, P., Feiz, A.-A., Ngae, P., Singh, S.K., Issartel, J.-P., 2015. CFD simulation of short-range plume dispersion from a point release in an urban like environment. Atmospheric Environment 122, 645–656. https://doi.org/10.1016/j.atmosenv.2015.10.027

Leelőssy, Á., Molnár, F., Izsák, F., Havasi, Á., Lagzi, I., Mészáros, R., 2014. Dispersion modeling of air pollutants in the atmosphere: a review. Open Geosciences 6, 257–278. https://doi.org/10.2478/s13533-012-0188-6

Liu, C., Bao, Q., Nie, W., 2022. The influence of ventilation parameters on dust pollution in a tunnel's environment using the CFD method. Journal of Wind Engineering and Industrial Aerodynamics 230, 105173. https://doi.org/10.1016/j.jweia.2022.105173

Nazarian, N., Kleissl, J., 2015. CFD simulation of an idealized urban environment: Thermal effects of geometrical characteristics and surface materials. Urban Climate 12, 141–159. https://doi.org/10.1016/j.uclim.2015.03.002

Nuvolone, D., Petri, D., Voller, F., 2018. The effects of ozone on human health. Environ Sci Pollut Res 25, 8074–8088. https://doi.org/10.1007/s11356-017-9239-3

Papageorgakis, G.C., Assanis, D.N., 1999. COMPARISON OF LINEAR AND NONLINEAR RNG-BASED k-epsilon MODELS FOR INCOMPRESSIBLE TURBULENT FLOWS. Numerical Heat Transfer, Part B: Fundamentals 35, 1–22. https://doi.org/10.1080/104077999275983

Petters, A., von Klot, S., Heier, M., Trentinaglia, I., 2004. Exposure to Traffic and the Onset of Myocardial Infarction. The New England Journal of Medicine 351, 1721–1730. https://doi.org/10.1056/NEJMoa040203

Reiminger, N., Jurado, X., Vazquez, J., Wemmert, C., Blond, N., Dufresne, M., Wertel, J., 2020a. Effects of wind speed and atmospheric stability on the air pollution reduction rate induced by noise barriers. Journal of Wind Engineering and Industrial Aerodynamics 200, 104160. https://doi.org/10.1016/j.jweia.2020.104160

Reiminger, N., Jurado, X., Vazquez, J., Wemmert, C., Blond, N., Wertel, J., Dufresne, M., 2020b. Methodologies to assess mean annual air pollution concentration combining numerical results and wind roses. Sustainable Cities and Society 59, 102221. https://doi.org/10.1016/j.scs.2020.102221

Reiminger, N., Vazquez, J., Blond, N., Dufresne, M., Wertel, J., 2020c. CFD evaluation of mean pollutant concentration variations in step-down street canyons. Journal of Wind Engineering and Industrial Aerodynamics 196, 104032. https://doi.org/10.1016/j.jweia.2019.104032

Richards, P.J., Hoxey, R.P., 1993. Appropriate boundary conditions for computational wind engineering models using the k-E turbulence model 9.

Richards, P.J., Norris, S.E., 2011. Appropriate boundary conditions for computational wind engineering models revisited. Journal of Wind Engineering and Industrial Aerodynamics 99, 257–266. https://doi.org/10.1016/j.jweia.2010.12.008

Rivas, E., Santiago, J.L., Lechón, Y., Martín, F., Ariño, A., Pons, J.J., Santamaría, J.M., 2019. CFD modelling of air quality in Pamplona City (Spain): Assessment, stations spatial representativeness and health impacts valuation. Science of the Total Environment 19.

Sanchez, B., Santiago, J.L., Martilli, A., Martin, F., Borge, R., Quaassdorff, C., de la Paz, D., 2017. Modelling NOX concentrations through CFD-RANS in an urban hot-spot using high resolution traffic emissions and meteorology from a mesoscale model. Atmospheric Environment 163, 155–165. https://doi.org/10.1016/j.atmosenv.2017.05.022

Sanchez, B., Santiago, J.-L., Martilli, A., Palacios, M., Kirchner, F., 2016. CFD modeling of reactive pollutant dispersion in simplified urban configurations with different chemical mechanisms. Atmos. Chem. Phys. 16, 12143–12157. https://doi.org/10.5194/acp-16-12143-2016

Santiago, J.-L., Buccolieri, R., Rivas, E., Sanchez, B., Martilli, A., Gatto, E., Martín, F., 2019. On the Impact of Trees on Ventilation in a Real Street in Pamplona, Spain. Atmosphere 10, 697. https://doi.org/10.3390/atmos10110697

Santiago, J.L., Martin, F., 2005. Modelling the air flow in symmetric and asymmetric street canyons. International Journal of Environment and Pollution 25, 145. https://doi.org/10.1504/IJEP.2005.007662

Solazzo, E., Vardoulakis, S., Cai, X., 2011. A novel methodology for interpreting air quality measurements from urban streets using CFD modelling. Atmospheric Environment 45, 5230–5239. https://doi.org/10.1016/j.atmosenv.2011.05.022

Soulhac, L., Mejean, P., Perkins, R.J., 2001. Modelling the transport and dispersion of pollutants in street canyons. International Journal of Environment and Pollution 16, 404. https://doi.org/10.1504/IJEP.2001.000636

Tominaga, Y., Stathopoulos, T., 2017. Steady and unsteady RANS simulations of pollutant dispersion around isolated cubical buildings: Effect of large-scale fluctuations on the concentration field. Journal of Wind Engineering and Industrial Aerodynamics 165, 23–33. https://doi.org/10.1016/j.jweia.2017.02.001

Tominaga, Y., Stathopoulos, T., 2007. Turbulent Schmidt numbers for CFD analysis with various types of flowfield. Atmospheric Environment 41, 8091–8099. https://doi.org/10.1016/j.atmosenv.2007.06.054

Toparlar, Y., Blocken, B., Maiheu, B., van Heijst, G.J.F., 2017. A review on the CFD analysis of urban microclimate. Renewable and Sustainable Energy Reviews 80, 1613–1640. https://doi.org/10.1016/j.rser.2017.05.248

Trindade da Silva, F., Reis, N.C., Santos, J.M., Goulart, E.V., Engel de Alvarez, C., 2021. The impact of urban block typology on pollutant dispersion. Journal of Wind Engineering and Industrial Aerodynamics 210, 104524. https://doi.org/10.1016/j.jweia.2021.104524

Troen, I., Petersen, E.L., 1989. European wind atlas. Published for the Commission of the European Communities, Directorate-General for Science, Research, and Development, Brussels, Belgium by Risø National Laboratory, Roskilde, Denmark.

United Nations, 2019. World Urbanization Prospects: The 2018 Revision (ST/ESA/SER.A/420). New York: United Nations.

Wang, X., McNamara, K.F., 2006. Evaluation of CFD Simulation using RANS Turbulence Models for Building Effects on Pollutant Dispersion. Environmental Fluid Mechanics 6, 181–202. https://doi.org/10.1007/s10652-005-5656-9

Wang, Y., Zhong, K., Zhang, N., Kang, Y., 2014. Numerical Analysis of Solar Radiation Effects on Flow Patterns in Street Canyons. Engineering Applications of Computational Fluid Mechanics 8, 252–262. https://doi.org/10.1080/19942060.2014.11015511

Wei, P., Brimblecombe, P., Yang, F., Anand, A., Xing, Y., Sun, L., Sun, Y., Chu, M., Ning, Z., 2021. Determination of local traffic emission and non-local background source contribution to on-road air pollution using fixed-route mobile air sensor

network. Environmental Pollution 290, 118055. https://doi.org/10.1016/j.envpol.2021.118055

WHO, 2021. WHO global air quality guidelines: particulate matter (PM2.5 and PM10), ozone, nitrogen dioxide, sulfur dioxide and carbon monoxide. World Health Organization.

WHO, 2017. Evolution of WHO air quality guidelines past, present and future, Copenhagen: WHO Regional Office for Europe.

WHO, 2016. Mortality and burden of disease from ambient air pollution, Global Health Observatory data [WWW Document]. Word Health Organization. URL http://www.who.int/gho/phe/outdoor_air_pollution/burden/en/ (accessed 11.20.19).

WHO (Ed.), 2005. WHO Air quality guidelines for particulate matter, ozone, nitrogen dioxide and sulfur dioxide. Global update 2005. World Health Organization.

Woodward, J.L., 1998. Estimating the flammable mass of a vapor cloud, A CCPS concept book. Center for Chemical Process Safety of the American Institute of Chemical Engineers, New York, N.Y.

Yakhot, V., Orszag, S.A., Thangam, S., Gatski, T.B., Speziale, C.G., 1992. Development of turbulence models for shear flows by a double expansion technique. Physics of Fluids A: Fluid Dynamics 4, 1510–1520. https://doi.org/10.1063/1.858424

Yang, J., Shi, B., Shi, Y., Marvin, S., Zheng, Y., Xia, G., 2020. Air pollution dispersal in high density urban areas: Research on the triadic relation of wind, air pollution, and urban form. Sustainable Cities and Society 54, 101941. https://doi.org/10.1016/j.scs.2019.101941

Yuan, Y., Yang, K., Du, C., Fu, X., 2017. Study on Schmidt Number of Pollutant Diffusion in Urban Street Atmosphere. Procedia Engineering 205, 1711–1717. https://doi.org/10.1016/j.proeng.2017.10.368

Zheng, X., Montazeri, H., Blocken, B., 2021. Large-eddy simulation of pollutant dispersion in generic urban street canyons: Guidelines for domain size. Journal of Wind Engineering and Industrial Aerodynamics 211, 104527. https://doi.org/10.1016/j.jweia.2021.104527